

Electronic structure and magnetism in UGa_2 : DFT+DMFT approach

Banhi Chatterjee^{1,2} and Jindřich Kolorenč^{1,*}

¹*Institute of Physics (FZU), Czech Academy of Sciences, Na Slovance 2, 182 21 Prague, Czech Republic*

²*Jožef Stefan Institute, Jamova 39, SI-1000 Ljubljana, Slovenia*

(Dated: January 4, 2022)

The debate whether uranium 5f electrons are closer to being localized or itinerant in the ferromagnetic compound UGa_2 is not yet fully settled. The experimentally determined magnetic moments are large, approximately $3 \mu_B$, suggesting the localized character of the 5f electrons. In the same time, one can identify signs of itinerant as well as localized behavior in various spectroscopic observations. The band theory, employing local exchange-correlation functionals, is biased toward itinerant 5f states and severely underestimates the moments. Using material-specific dynamical mean-field theory (DMFT), we probe how a less approximate description of electron-electron correlations improves the picture. We present two variants of the theory: starting either from spin-restricted (LDA) or spin-polarized (LSDA) band structure. We show that the L(S)DA+DMFT method can accurately describe the magnetic moments in UGa_2 as long as the exchange interaction between the uranium 6d and 5f electrons is preserved by a judicious choice of the spin-polarized double-counting correction. We discuss the computed electronic structure in relation to photoemission experiments and show how the correlations reduce the Sommerfeld coefficient of the electronic specific heat by shifting the 5f states slightly away from the Fermi level.

I. INTRODUCTION

The 5f electrons in actinides and their compounds can be either itinerant and participating in chemical bonds, or localized and not contributing to cohesion. A transition akin to Mott metal-insulator transition occurs in elemental actinide metals between Pu and Am [1]. Although elemental uranium has itinerant 5f electrons, its compounds display both types of 5f states. A traditional way of classifying uranium compounds is by placing them in the Hill plot that relates the critical temperature (magnetic or superconducting) to the nearest neighbor U–U spacing [2]. Small U–U distances favor superconducting behavior at low temperatures, whereas long-range magnetic order takes place at spacings greater than the so-called Hill limit (3.5 Å).

In UGa_2 , an intermetallic binary compound with a hexagonal AlB_2 structure (space group $P6/\text{mmm}$, Fig. 1), the Ga atoms effectively separate the uranium atoms, increasing the U–U distance to 4.0 Å, that is, above the Hill limit. Accordingly, the compound exhibits ferromagnetic order below $T_C = 125$ K with the easy magnetization axis along the [100] direction. Experimental observations establish magnetic moments of approximately $3 \mu_B$ per U atom in the ferromagnetic phase, using magnetization measurements [3, 4] as well as neutron diffraction [5, 6]. UGa_2 thus exhibits moments and ordering temperature that are larger than typical for ferromagnetic uranium intermetallics [7], which indicates localized 5f electrons. The magnetic behavior can indeed be accurately reproduced by a fully local crystal-field model corresponding to the $5f^3$ configuration of the U ion [8]. In addition, the observed Sommerfeld coefficient $\gamma = 11$ mJ/mol·K² [9] is not much enhanced compared to the analogous compound without 5f electrons – LaGa_2 , displaying $\gamma = 4$ mJ/mol·K² [10], which testifies against a high density of electronic states at the Fermi level in UGa_2 , again favoring the localized

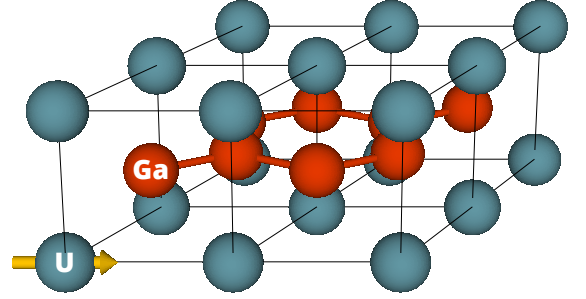


FIG. 1. The hexagonal lattice of UGa_2 with uranium atoms shown in blue and gallium atoms in red. The uranium magnetic moments (arrow) are aligned along the [100] direction.

picture of the 5f electrons. The spectroscopic evidence, on the other hand, is not conclusive about the nature of the 5f states since one can identify spectral features characteristic to localized electrons as well as features typical to itinerant electrons [11–13]. Similarly, the Fermi surface probed by the de Haas–van Alphen effect is not compatible with full 5f localization [9].

The large spin-orbit coupling (SOC), the crystal-field splitting, and the Coulomb interaction between the 5f electrons influence the magnetic moments in a non-trivial manner. This complexity contributes to the fact that the electronic structure of UGa_2 is not yet satisfactorily understood. The first-principles band theory based on semi-local approximations to the density-functional theory (DFT) severely underestimates the moments, yielding about $0.6 \mu_B$ per uranium atom [14, 15]. The correlated band theory incorporating an on-site Hubbard interaction term, DFT+ U , can successfully model the magnetically ordered states, particularly in insulating compounds with localized 5f electrons [16–18]. In UGa_2 , it enhances the magnetic moments up to $2.8 \mu_B$ but the spectroscopic results are not reproduced very well [15, 19].

The DFT+ U method is a static mean-field approximation and as such it cannot account for the multi-reference character of the 5f shell nor for dynamical many-body effects. These limitations are lifted when DFT is combined with the dynamical mean-field theory (DMFT) [20, 21], which accurately models both itinerant and localized electrons. In this paper, we investigate how the theoretical description of the magnetism and of the electronic structure of UGa₂ improves when the DFT+DMFT is applied. We estimate and discuss the effects of the 6d–5f exchange interactions on the 5f magnetic moments, and compare the computed spectral properties with the experimental valence-band photoemission spectra (PES). We also discuss technical matters pertaining to spin-polarized DFT+DMFT solutions.

II. METHOD

The DFT+DMFT method improves upon DFT+ U by replacing the static mean-field potential, approximating the Coulomb interaction among the uranium 5f electrons, with an energy-dependent (dynamical) potential (self-energy) [20, 22]. This self-energy is computed by solving an auxiliary impurity model – a many-body problem, for which we employ the exact diagonalization. We present two variants of the theory differentiated by the self-energy being inserted (a) into the spin-restricted LDA band structure (we call this method LDA+DMFT), and (b) into the ferromagnetic LSDA band structure (we refer to this variant as to LSDA+DMFT). A similar comparison of spin-restricted and spin-polarized parent band structures was performed for ferromagnetic nickel in [23].

A. General formalism

We start with determination of the first-principles band structure by means of the WIEN2k code [24] using parameters listed in Appendix A. Scalar relativistic effects as well as the spin-orbit coupling are included in these WIEN2k calculations [25]. Afterwards, the relevant valence bands are represented by a tight-binding Hamiltonian in the basis of the maximally-localized Wannier functions [26, 27]. This Hamiltonian is then used as the parent band structure for the DMFT calculations.

In each iteration of the DMFT self-consistency cycle, the local electronic structure around one shell of the uranium 5f Wannier functions is mapped onto a non-interacting impurity model (Appendix B),

$$\hat{H}_{\text{imp}} = \sum_{mm'\sigma\sigma'} [\mathbb{H}_{\text{loc}}]_{mm'}^{\sigma\sigma'} \hat{f}_{m\sigma}^\dagger \hat{f}_{m'\sigma'} + \sum_J \epsilon_J \hat{b}_J^\dagger \hat{b}_J + \sum_{m\sigma J} \left(V_{Jm\sigma} \hat{f}_{m\sigma}^\dagger \hat{b}_J + V_{Jm\sigma}^* \hat{b}_J^\dagger \hat{f}_{m\sigma} \right), \quad (1)$$

where $\hat{f}_{m\sigma}^\dagger$ creates an electron in the 5f shell with magnetic quantum number m and spin projection $\sigma \in \{-1/2, 1/2\}$

(eigenvalues of \hat{s}_z). The first term in Eq. (1) corresponds to the local Hamiltonian, which describes the 5f shell. It can be decomposed as

$$\mathbb{H}_{\text{loc}} = \epsilon_f \hat{I} + \zeta \hat{\mathbf{I}} \cdot \hat{\mathbf{s}} - \hat{\mathbf{s}} \cdot \boldsymbol{\Delta}_X + B_{20} \hat{O}_{20} + B_{40} \hat{O}_{40} + B_{60} \hat{O}_{60} + B_{66} \hat{O}_{66}, \quad (2)$$

where ϵ_f is the energy of the 5f level, ζ is the strength of the SOC, $\boldsymbol{\Delta}_X$ gives the exchange splitting, and \hat{O}_{kq} and B_{kq} are Stevens operators and the corresponding parameters that characterize the D_{6h} crystal-field potential at the uranium site in UGa₂. In general, the parameters B_{kq} can be spin dependent, which we briefly discuss at the end of Appendix C. Note that the decomposition introduced in Eq. (2) is only used for the analysis of \mathbb{H}_{loc} and has no influence on the DMFT calculations and results.

The second term in Eq. (1) corresponds to an effective medium usually referred to as the bath, with which the 5f shell interacts. The operator \hat{b}_J^\dagger creates an electron in this effective medium. The last term in Eq. (1) accounts for the hybridization of the 5f shell with the bath. In our calculations, the off-diagonal hybridization induced by the non-commutativity of the hexagonal symmetry with the SOC is fully taken into account. The crystal-field splitting of the 5f states is partly due to the crystal-field potential contained in \mathbb{H}_{loc} and partly due to the hybridization.

The full interacting impurity model, in which the self-energy is computed, is given by

$$\hat{H}_{\text{imp}}^{\text{DMFT}} = \hat{H}_{\text{imp}} + \hat{U}, \quad (3)$$

where \hat{H}_{imp} is the non-interacting one-electron part shown in Eq. (1) and \hat{U} is the Coulomb repulsion among the 5f electrons,

$$\hat{U} = \frac{1}{2} \sum_{\substack{mm'm''m''' \\ m'''\sigma\sigma'}} U_{mm'm''m'''} \hat{f}_{m\sigma}^\dagger \hat{f}_{m'\sigma'}^\dagger \hat{f}_{m''\sigma''} \hat{f}_{m'''\sigma'''} - \sum_{m\sigma} (U_H - \sigma U_X) \hat{f}_{m\sigma}^\dagger \hat{f}_{m\sigma}, \quad (4)$$

where $U_{mm'm''m'''}$ is considered in its full spherically symmetric form parametrized by four Slater integrals $F_0 = 2.0$ eV, $F_2 = 7.09$ eV, $F_4 = 4.60$ eV, and $F_6 = 3.36$ eV, which correspond to Coulomb $U = 2.0$ eV and Hund $J = 0.59$ eV. The first integral, F_0 , is at the upper limit, beyond which the 5f peak in the occupied LSDA+ U density of states moves too far from the Fermi level to be compatible with the valence-band photoemission spectra [11, 15]. The other three parameters (F_2 , F_4 , F_6) correspond to the atomic Hartree–Fock values calculated for the U³⁺ ion (5f³ configuration) and then reduced to 80% to mimic screening [28, 29]. Note that the unscreened ionic F_k values yield Hund $J = 0.79$ eV, which can be considered as the maximal value for the uranium 5f³ systems.

The second term in Eq. (4) is the double-counting correction introduced to remove the static mean-field approximation of the 5f–5f Coulomb interaction that is

incorporated in the DFT band structure. We assume the double-counting correction to be spherically symmetric (neither U_H nor U_X depends on the magnetic quantum number m), with $U_X = 0$ for the LDA band structure and $U_X \neq 0$ for the LSDA band structure. The numerical values of U_H and U_X are discussed later in Secs. II C and II D.

The impurity model, Eq. (3), is solved using the exact diagonalization (Lanczos) method [30, 31] as implemented in our in-house code [32]. The size of the models, which can be solved by this method, is limited due to unfavorable scaling of the computational demands. The impurity models employed in this paper consist of 14 spinorbitals corresponding to the 5f shell and another 42 spinorbitals representing the bath. Of the bath states, $N_b^< = 14$ orbitals have ϵ_J below the Fermi level (they are nominally occupied) and $N_b^> = 28$ orbitals have ϵ_J above the Fermi level (they are nominally empty). Even these small models are too demanding unless we turn to a reduction of the many-body basis inspired by the work of Gunnarsson and Schönhammer [32, 33]. A cutoff M is introduced for each N -electron Hilbert space \mathcal{H}_N , and the diagonalization is performed only in a subspace

$$\mathcal{H}_N^{(M)} = \{|f^{N-N_b^<-n+m} b^n \underline{b}^m\rangle, 0 \leq m+n \leq M\}. \quad (5)$$

In this notation, $f^{N-N_b^<-n+m}$ indicates $N - N_b^< - n + m$ electrons in the uranium 5f shell, b^n indicates n electrons in the bath orbitals above the Fermi level, and \underline{b}^m means m holes in the bath orbitals below the Fermi level. We use $M = 2$ for the cutoff. The convergence with respect to M is discussed in Appendix D.

The impurity solver yields a self-energy $[\hat{\Sigma}(z)]_{mm'}^{\sigma\sigma'}$, acting in the subspace of 5f spinorbitals, which enters the Dyson equation for the local Green's function $\hat{G}(z)$,

$$\hat{G}(z) = \frac{1}{\mathcal{N}} \sum_{\mathbf{k}} [z\hat{I} - \hat{H}_{\mathbf{k}} - \hat{\Sigma}(z)]^{-1}, \quad (6)$$

where \mathcal{N} is the number of \mathbf{k} points in the Brillouin zone (4096 in our calculations) and $\hat{H}_{\mathbf{k}}$ is the tight-binding Hamiltonian. The local Green's function determines an updated impurity model (Appendix B), concluding one iteration of the DMFT cycle.

After the DMFT self-consistency is reached, the occupation matrix of the 5f states is evaluated from the 5f block of the local Green's function,

$$\hat{n}_f = \int_{-\infty}^{E_F} \hat{A}_f(\epsilon) d\epsilon, \quad \hat{A}_f(\epsilon) = -\frac{1}{\pi} \text{Im} \hat{G}_f(\epsilon + i0), \quad (7)$$

where the integral runs over all occupied states up to the Fermi energy E_F . Knowing the occupation matrix, we can calculate the 5f electron occupation as well as spin and orbital moments as averages of the corresponding operators,

$$n_f = \text{Tr}(\hat{n}_f) \quad \text{and} \quad \langle O \rangle = \text{Tr}(\hat{O} \hat{n}_f). \quad (8)$$

Finally, the Sommerfeld coefficient of the electronic specific heat γ is evaluated using the Fermi-liquid formula,

$$\gamma = \frac{\pi k_B^2}{3} \left[\frac{g_f(E_F)}{Z_f} + g_{spd}(E_F) \right], \quad (9)$$

where $g_f(E_F) = \text{Tr}[\hat{A}_f(E_F)]$ is the density of 5f states at the Fermi energy, $g_{spd}(E_F)$ is the density of all other states at the Fermi energy, and $Z_f < 1$ is the average quasiparticle weight in the 5f bands that is estimated from the DMFT self-energy as suggested in [34],

$$\frac{1}{Z_f} = \text{Tr} \left[\frac{\hat{A}_f(E_F)}{g_f(E_F)} \left(\hat{I} - \frac{d\hat{\Sigma}(\epsilon + i0)}{d\epsilon} \right) \right]_{\epsilon=E_F}. \quad (10)$$

All DMFT calculations presented in this paper are performed at temperature $T = 0$ K in order to obtain the ferromagnetic state with saturated magnetic moments.

B. Choice of the tight-binding model

We investigated several tight-binding models $\hat{H}_{\mathbf{k}}$ of increasing size. As the minimal model, we considered one that contains gallium 4s and 4p, and uranium 5f and 6d states. Then we included uranium 7s and finally also 7p states. Various characteristics of these models are listed in Table I. Although the uranium 7p states are relatively high above the Fermi level, their inclusion makes a sizable difference, in particular to the crystal-field parameters in \mathbb{H}_{loc} and to the filling of the gallium states.

On the top of that, we found that the LDA+DMFT calculations without the U 7p states converge to the out-of-plane [001] ferromagnetic state, whereas the calculations with the U 7p states predict an in-plane ferromagnetic state. Since the experiments determine UGa_2 to be an in-plane ferromagnet [3, 4], all results presented in the following sections were obtained in the tight-binding models that include uranium 7s and 7p states.

C. LDA+DMFT

When the parent band structure is spin-restricted (LDA), we induce the ferromagnetic solution by introducing a small symmetry-breaking magnetic field into the impurity model, Eq. (1), in the first few iterations of the DMFT self-consistency cycle. Afterwards, this field is removed again. Since we do not implement any charge self-consistency, the tight-binding Hamiltonian $\hat{H}_{\mathbf{k}}$ remains unchanged during the whole LDA+DMFT cycle and the spin (and orbital) polarization is introduced only by means of the polarized self-energy applied to the 5f states. This method very likely results in an underestimated spin polarization of the 6d bands. Moreover, the local Hamiltonian \mathbb{H}_{loc} stays non-polarized as demonstrated in Appendix C, that is, no exchange field Δ_X is induced in \mathbb{H}_{loc} by the polarized self-energy. Nevertheless,

TABLE I. Characteristics of several tight-binding models derived from the DFT band structure. All models contain gallium 4s and 4p orbitals, the included uranium orbitals are listed in the first column. The quantities ζ , ϵ_f and Δ_X are shown in eV, the crystal-field parameters B_{kq} in meV.

| model | orbital occupations | | | | | | | | local Hamiltonian \mathbb{H}_{loc} | | | | | | | |
|------------------------------|---------------------|-----------------|-------------------|-----------------|-------------------|------|------|-------|---|---------|--------------|------------|----------|----------|----------|----------|
| | U 5f | U 5f \uparrow | U 5f \downarrow | U 6d \uparrow | U 6d \downarrow | U 7s | U 7p | Ga 4s | Ga 4p | ζ | ϵ_f | Δ_X | B_{20} | B_{40} | B_{60} | B_{66} |
| nonmagnetic solution | | | | | | | | | | | | | | | | |
| d,f | 2.79 | | | 0.94 | 0.94 | – | – | 1.51 | 2.18 | 0.248 | 0.634 | 0 | –0.72 | –0.14 | 0.00 | –0.19 |
| s,d,f | 2.77 | | | 0.95 | 0.95 | 0.35 | – | 1.50 | 2.03 | 0.248 | 0.639 | 0 | –0.69 | –0.12 | –0.01 | –0.16 |
| s,p,d,f | 2.72 | | | 1.03 | 1.03 | 0.76 | 0.74 | 1.39 | 1.50 | 0.251 | 0.679 | 0 | –2.83 | –0.01 | 0.00 | –0.06 |
| ferromagnetic solution [001] | | | | | | | | | | | | | | | | |
| s,d,f | 2.77 | 2.41 | 0.37 | 1.00 | 0.87 | 0.35 | – | 1.49 | 2.02 | 0.246 | 0.926 | 0.972 | 5.98 | –0.11 | –0.01 | –0.16 |
| s,p,d,f | 2.72 | 2.37 | 0.36 | 1.08 | 0.96 | 0.76 | 0.74 | 1.39 | 1.49 | 0.249 | 0.968 | 0.980 | 3.71 | 0.01 | 0.00 | –0.05 |
| ferromagnetic solution [210] | | | | | | | | | | | | | | | | |
| s,p,d,f | 2.72 | 2.34 | 0.38 | 1.08 | 0.95 | 0.76 | 0.74 | 1.34 | 1.54 | 0.248 | 0.956 | 0.956 | 3.92 | 0.03 | 0.00 | –0.04 |

there should be some exchange field present in \mathbb{H}_{loc} due to the partially filled and partially polarized 6d bands, and neglecting this exchange certainly means underestimated 5f moments (which is indeed what we observe in Sec. III A). We fix this deficiency by introducing an empirical exchange field Δ_{fd} analogously to the earlier computational studies of rare-earth systems [35, 36]. The magnitude of this field is estimated as $\Delta_{fd} \approx I_{fd}m_d$ [35], where m_d is the magnetic moment due to the 6d electrons and I_{fd} is intra-atomic exchange integral. The magnetic moment is approximated by its LSDA value, $m_d \approx 0.24 \mu_B$ (see Table I for the spin-resolved filling of the 6d bands), the exchange integral is estimated by atomic calculations, $I_{fd} \approx 0.15 \text{ eV}/\mu_B$ [37]. This yields $I_{fd}m_d \approx 36 \text{ meV}$ and we explore the LDA+DMFT solutions for Δ_{fd} varied around this value.

The absence of Δ_X is a disadvantage of the spin-restricted parent band structure. Its advantage, on the other hand, is that the double-counting correction in Eq. (4) reduces to a single number, U_H , since the spin-dependent part, U_X , vanishes. One possible approximation to the double counting is the so-called fully localized limit (FLL),

$$U_H^{\text{FLL}} = U(n_f - 1/2) - J(n_f - 1)/2, \quad (11)$$

where n_f is the self-consistently determined number of 5f electrons [16, 38]. In our calculations, it turned out that this U_H^{FLL} severely overestimates the number of 5f electrons, resulting in $n_f \approx 4$. We hence employ an alternative strategy: we choose U_H such that the number of 5f electrons remains close to its LDA value ($n_f = 2.72$, Table I) also in the LDA+DMFT solution to simulate charge self-consistency [39, 40]. This condition implies $U_H \approx 3 \text{ eV}$. We note in passing that the FLL formula, Eq. (11), gives 3.93 eV for $n_f = 2.72$, 4.41 eV for $n_f = 3$, and 2.71 eV for $n_f = 2$.

D. LSDA+DMFT

As discussed above, using spin-restricted LDA as the parent band structure has two deficiencies: underestimated spin polarization of the 6d (and other) bands, and missing exchange field due to 6d moments acting on the 5f electrons. We dealt with the second issue empirically, but we did not address the first one yet. We attempt to do so by using the spin-polarized (LSDA) solution as the parent band structure. This way, all non-5f bands are potentially spin-polarized, which enhances the polarization of the bath and of the bath–5f hybridization in the auxiliary impurity model, Eq. (1), when compared to LDA+DMFT described in Sec. II C.

Although it may seem that the LSDA parent band structure also provides an improved estimate of the local exchange field Δ_X , it is not so, since the LSDA exchange field combines the 6d–5f exchange (tens of meV) with the 5f–5f exchange (about 1 eV). The latter has to be removed by the double-counting correction U_X , which we know only approximately. The FLL ansatz for the double counting U_X reads as [16]

$$U_X^{\text{FLL}} = E_{\text{FLL}}^\downarrow - E_{\text{FLL}}^\uparrow = J(n_f^\uparrow - n_f^\downarrow), \quad (12)$$

where

$$E_{\text{FLL}}^\sigma = U(n_f - 1/2) - J(n_f^\sigma - 1/2), \quad (13)$$

which we find to overcorrect the LSDA 5f–5f exchange. With the LSDA occupation numbers (Table I) and with $J = 0.59 \text{ eV}$, the double counting U_X^{FLL} becomes 1.19 eV whereas the LSDA exchange is only $\Delta_X = 0.98 \text{ eV}$ (Table I).

Instead of using Eq. (12) or any other similar formula, we again employ the approach introduced in Sec. II C, that is, we select U_X such that $\Delta_{fd} = \Delta_X - U_X \approx I_{fd}m_d \approx 36 \text{ meV}$. Since Δ_X is a parameter of the local Hamiltonian, it remains constant during the DMFT self-consistency

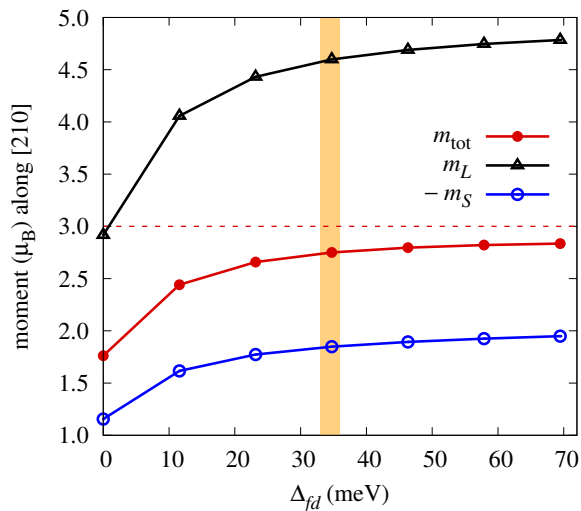


FIG. 2. The total magnetic moment (red), the orbital (black) and spin (blue) contributions to the magnetic moment of the 5f shell as functions of the exchange field Δ_{fd} applied along the [210] direction in the LDA+DMFT calculations. The realistic value of Δ_{fd} is marked by the orange stripe, the experimental magnetic moment is indicated by the dashed line [4].

iterations as follows from the derivation presented in Appendix C, hence Δ_{fd} and U_X remain constant as well.

For the spin-independent part of the double-counting correction, we choose $U_H = 3.3$ eV. This value is 0.3 eV larger than in LDA+DMFT because the average position of the 5f level is approximately 0.3 eV higher in the ferromagnetic LSDA solution compared to the non-magnetic LDA solution (Table I).

III. RESULTS

A. Magnetic moments

The method outlined in the preceding sections is not entirely self-contained – there are several semi-empirical parameters, such as the Coulomb parameters F_k , the double-counting correction U_H , and the exchange field Δ_{fd} . Especially the exchange field was estimated only roughly and hence we decided to explore a range of values around this estimate.

In Figure 2 we show how the magnetic moments depend on Δ_{fd} in the LDA+DMFT calculations when Δ_{fd} is applied in plane, along the [210] direction, which corresponds to the [210] ferromagnetic state [41]. The orbital and spin contributions to the magnetic moment are antiparallel as expected for 5f filling smaller than 7. At $\Delta_{fd} = 0$ meV, the total magnetic moment is clearly underestimated ($1.76 \mu_B$), which confirms our earlier reasoning that some exchange field has to be introduced. As the exchange field increases, the magnetic moment quickly increases too, it reaches $2.75 \mu_B$ at $\Delta_{fd} = 35$ meV, at which point it is

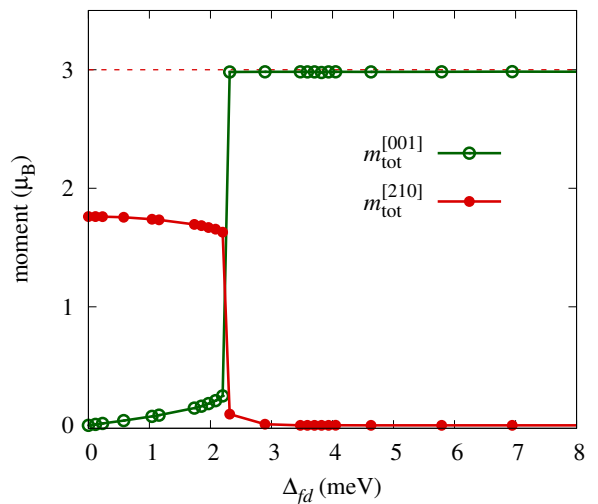


FIG. 3. Projection of the total magnetic moment to the [210] direction (red) and to the [001] direction (green) when the exchange field Δ_{fd} is applied along the [001] direction and the LDA+DMFT calculations are started from the LDA solution with $\Sigma(z) = 0$. The orbital and spin moments (not shown) behave similarly as in Fig. 2.

already very close to the saturation value $\approx 2.88 \mu_B$. The quick saturation of the moments is a convenient feature – an inaccuracy in estimating the realistic value of Δ_{fd} translates to only a minor uncertainty of the computed magnetic moments. The moments and 5f filling at the realistic value of Δ_{fd} are compared to the LSDA solution and to experiments in Table II.

Analogous calculations were performed also for the exchange field Δ_{fd} applied along the out-of-plane [001] direction. In this case, the ferromagnetic state parallel to the exchange field is stable only above some critical value of Δ_{fd} , see Fig. 3. Above this value, the magnetic moment very quickly saturates, much faster than in Fig. 2. For

TABLE II. The orbital and spin magnetic moments in uranium 5f shells, m_S and m_L (in μ_B), the total magnetic moment in the unit cell m_{tot} (in μ_B), the occupation of the 5f shells n_f , and the Sommerfeld coefficient γ (in mJ/mol·K²). The moments and the 5f filling correspond to the maximally localized Wannier functions. The experimental m_{tot} is taken from [4], the experimental γ from [9].

| | U_H | Δ_{fd} | dir. | m_S | m_L | m_{tot} | n_f | γ |
|------------|-------|---------------|-------|-------|-------|-----------|-------|----------|
| LSDA | – | – | [210] | –1.96 | 2.79 | 0.65 | 2.72 | 24.5 |
| LSDA | – | – | [001] | –2.00 | 2.89 | 0.70 | 2.72 | 21.2 |
| LDA+DMFT | 3.0 | 35 | [210] | –1.85 | 4.60 | 2.75 | 2.76 | 8.2 |
| LDA+DMFT | 3.0 | 35 | [001] | –1.91 | 4.87 | 2.96 | 2.74 | 7.7 |
| LSDA+DMFT | 3.3 | 35 | [210] | –1.66 | 4.15 | 2.30 | 2.82 | 7.2 |
| LSDA+DMFT | 3.3 | 35 | [001] | –1.59 | 3.89 | 2.12 | 2.80 | 7.5 |
| experiment | | | | | | 3.07 | | 11.0 |

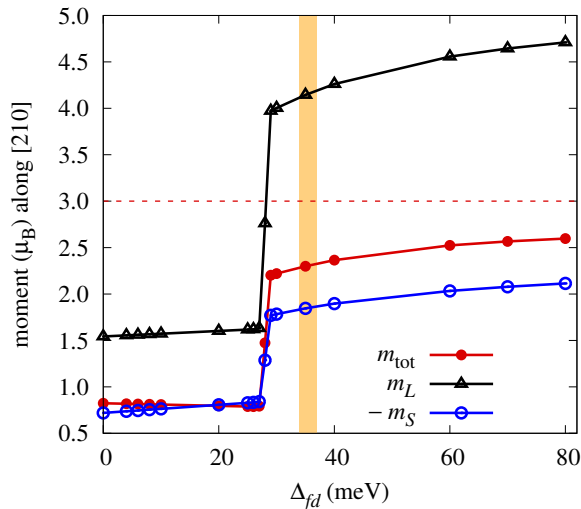


FIG. 4. Variation of magnetic moments with Δ_{fd} , computed using the LSDA+DMFT method when the parent band structure is polarized in the [210] direction. Compare with Fig. 2.

smaller values of Δ_{fd} , the DMFT iterations converge to a nearly in-plane state with just a small out-of-plane tilt of the magnetic moments. For a range of Δ_{fd} values we get two stationary solutions, one nearly in-plane and the other out-of-plane, depending on the starting point of the DMFT iterations. Figure 3 shows calculations that were started at a given Δ_{fd} from the LDA state with $\Sigma(z) = 0$. The transition from the in-plane to out-of-plane state then occurs at $\Delta_{fd} \approx 2.2$ meV. Calculations starting from the [001] ferromagnetic state converge to the out-of-plane state already at $\Delta_{fd} \gtrsim 0.6$ meV (not shown).

Unfortunately, we cannot determine which of the two stationary states found for Δ_{fd} between 0.6 meV and 2.2 meV is the ground state because we cannot reliably evaluate the total energy in our LDA+DMFT implementation. For the same reason, we cannot estimate the magnetocrystalline anisotropy energy. We can, however, conclude that the response of the magnetic moments to Δ_{fd} as observed in LDA+DMFT is consistent with the experimental finding that the easy axis is oriented in plane. Starting from the paramagnetic state ($\Delta_{fd} = 0$) and cooling down, the system always ends up in the in-plane state, since the moments exhibit an instability toward in-plane direction. Increasing in-plane moment increases in-plane Δ_{fd} , which stabilizes the in-plane state further.

The magnetic moments computed using LSDA+DMFT, with the spin-dependent part of the double-counting correction U_X varied to reproduce the same range of Δ_{fd} as explored above, are presented in Figs. 4 and 5 for the in-plane and out-of-plane orientation of the LSDA polarization. As in the LDA+DMFT, the total magnetic moments relatively quickly saturate with increasing Δ_{fd} , and the saturation is again faster in the [001] state than in the [210] state. Surprisingly, the saturated values of the total moments are noticeably smaller than in the

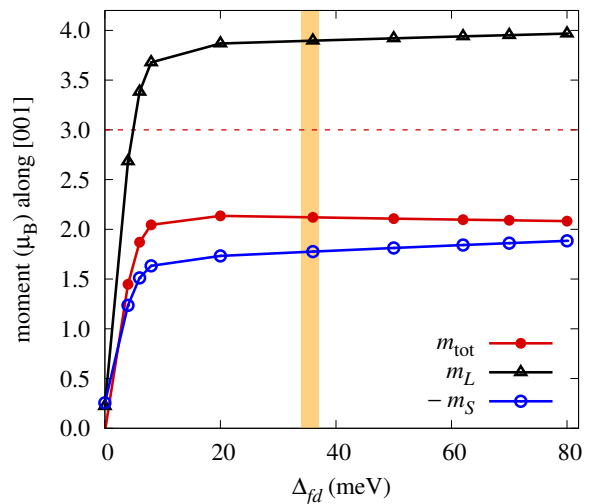


FIG. 5. The same plot as in Fig. 4, only the parent LSDA band structure is polarized in the [001] direction. To be compared with Fig. 3.

corresponding LDA+DMFT calculations, by 15% in the case of the [210] ferromagnet and by 30% in the case of the [001] ferromagnet (compare with Figs. 2 and 3). We expected the opposite, since the LSDA parent band structure is certainly more polarized than the LDA parent band structure – besides Δ_{fd} that is the same in both approaches by construction, the LSDA has all non-5f bands spin split, which results in an enhanced polarization of the hybridization function. Intuitively, this should have induced a larger polarization in the 5f shell but the calculations show that it does not.

The difference in the computed moments could in principle be due to a difference in fillings of the 5f shell between the LDA+DMFT and LSDA+DMFT solutions, but this is not the case either. The 5f filling in both methods is very close as can be checked in Table II where we summarize our results for the realistic setting of the exchange field Δ_{fd} . We speculate that the inaccurate LSDA+DMFT moments come from some artifact of the static LSDA approximation, possibly from an artificially broken symmetry. One suspect feature is the strong spin dependence of the crystal-field parameters B_{kq} in the local Hamiltonian shown in Appendix C. Another feature, for which we do not have a clear explanation and which is likely to be connected to the LSDA solution as well, is the jump in magnetic moments near $\Delta_{fd} = 30$ meV in Fig. 4.

Figures 2–5 show the computed magnetic moments as functions of the exchange field Δ_{fd} for a fixed spin-independent part of the double-counting correction U_H . Although the employed values of U_H are well justified in Secs. II C and II D, it is useful to analyze the sensitivity of the magnetic moments to changes of U_H or, equivalently, to changes of the 5f filling n_f . This sensitivity is illustrated in Fig. 6 for the [210] ferromagnetic state calculated with the LDA+DMFT method. The [001] ferromagnetic

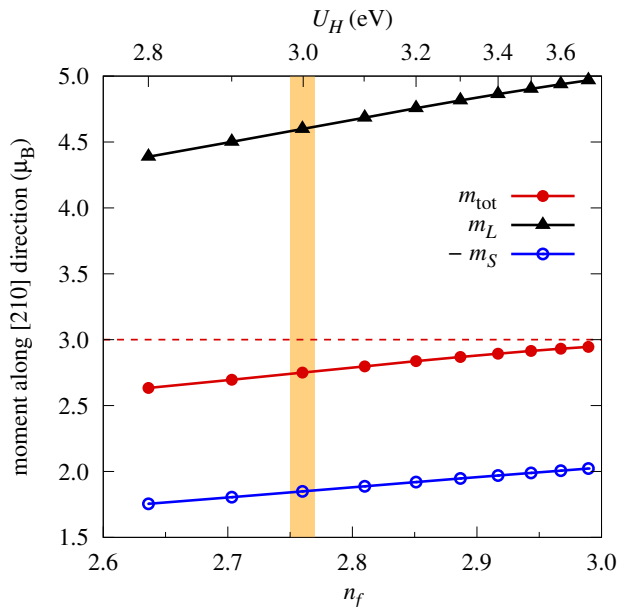


FIG. 6. The computed LDA+DMFT magnetic moments plotted as functions of the 5f filling n_f that is varied by changing the double-counting correction U_H . The exchange field $\Delta_{fd} = 35$ meV was applied along the [210] direction. The value $U_H = 3.0$ eV employed throughout the paper is marked by the orange stripe.

state and the results of the LSDA+DMFT method behave analogously. The magnetic moments increase toward the experimentally determined value with increasing n_f but this route to improved agreement with experiments does not have a solid physical backing. Moreover, it would come at the cost of worsened agreement with the spectroscopic measurements, since increased U_H would push the uranium 5f states to too large binding energies.

B. Valence-band spectroscopy

Two measurements of valence-band photoemission spectra of UGa_2 can be found in the literature, the ultraviolet photoemission spectrum [11] (UPS, shown in the left panel of Fig. 7) and the soft-x-ray photoemission spectrum [12] (SX-PES, shown in the middle panel of Fig. 7). The UPS was measured on sputter-deposited films at room temperature, that is, in the paramagnetic phase. The maximum intensity was observed just below the Fermi level with a long tail extending toward higher binding energies. The SX-PES was measured on a freshly cleaved single crystal at $T = 20$ K, that is, well below the Curie temperature. The spectrum shows a narrow peak slightly below the Fermi level accompanied with two broader features at -0.5 eV and -1.0 eV, and an even broader hump can be discerned at -2.8 eV.

The two spectra are clearly different and the difference cannot be ascribed to the lower resolution of the UPS spectra. The magnetic order is also unlikely to cause such

large changes, we certainly do not see any evidence of that in DFT+DMFT calculations (not shown), and the experiment does not detect any changes either [12]. The more probable source of the differences is the probing depth of the two experiments. The UPS used incident photons with energy 40.8 eV (He II line), SX-PES used 800 eV (synchrotron radiation), and hence the photoelectrons are emitted from deeper layers in the bulk of the sample in the SX-PES measurements.

Since our calculations do not include any surface effects, they should be closer to the SX-PES data. In Figure 7 we show our theoretically estimated photoelectron spectra at the appropriate photon energies, calculated for the [210] ferromagnetic phase with the LDA+DMFT method ($\Delta_{fd} = 35$ meV, but the spectra are not sensitive to variations of the 6d–5f exchange field). The spectra are constructed as linear combinations of the *orbital-resolved* densities of states (DOS) weighted with photoionization cross sections listed in [43]. According to these cross sections, the 5f DOS has by far the largest weight for both 40.8 eV and 800 eV photon energies, and hence these photoemission measurements probe mainly the 5f states.

The computed spectra display a main peak at -0.15 eV and a satellite at -0.8 eV. The satellite has a considerably smaller intensity than the features seen in the SX-PES and as such the theory appears to be closer to the UPS spectra. The -0.5 eV and -2.8 eV features observed in SX-PES do not show up in the theoretical PES, but there are distinct peaks appearing at nearby energies in the LDA+DMFT *total* DOS (Fig. 7). They originate from orbitals that have small photoionization cross sections. These peaks are due to hybridized U 6d and Ga 4p bands at -0.5 eV, and mainly Ga 4p bands at -2.4 eV. The distinct feature outside the range probed by photoemission, at -7.6 eV, is due to Ga 4s. The fact that SX-PES sees a signal where the theory places Ga 4p bands may be an indication that the theory underestimates the hybridization between Ga 4p and U 5f states. If the hybridization was stronger, some U 5f DOS would possibly appear at the position of the Ga 4p states, but that is just a speculation at this point.

Photoemission experiments access only the occupied part of the spectrum. The unoccupied part could be probed by inverse photoemission (we are not aware of any such experiment being performed to date) or by x-ray absorption spectroscopy (we discuss recent x-ray absorption measurements at the uranium $M_{4,5}$ edges in UGa_2 elsewhere [13]). In Figure 8, we analyze the complete (occupied and unoccupied) 5f DOS from a theoretical perspective. We compare the LDA+DMFT result with the DOS computed for a spherically symmetric $5f^3$ ion, since three is the closest integer value to the computed average 5f filling n_f (Table II) and the probability of finding the 5f shell in the $5f^3$ configuration predicted by LDA+DMFT is large, namely 83%. See Appendix D, Eq. (D1), for the meaning of the fluctuating number of 5f electrons. We can achieve a very close correspondence of the ionic and LDA+DMFT densities of states when the Coulomb U in

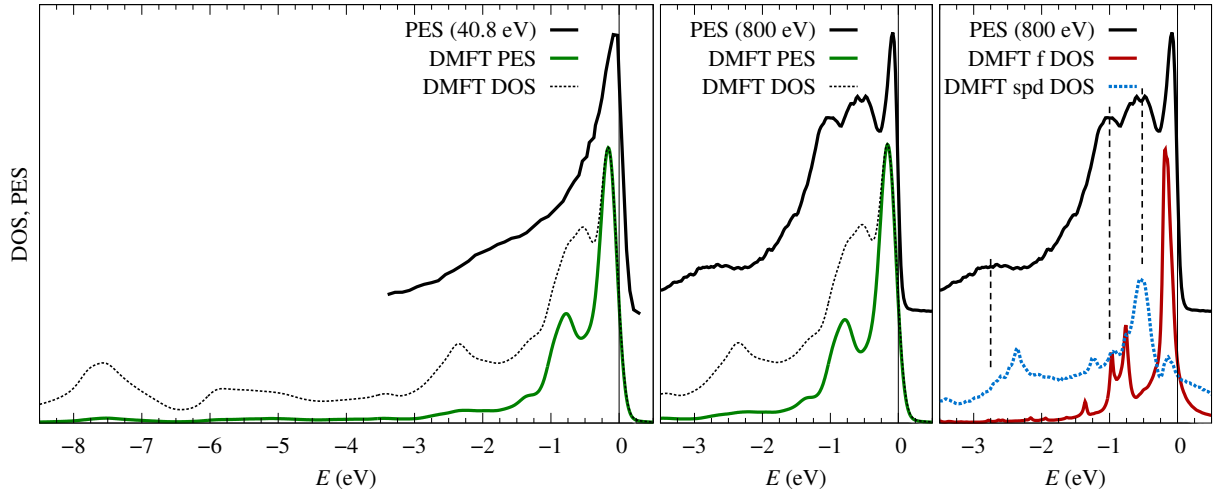


FIG. 7. Experimental photoelectron spectra (black line) from [11] (left panel) and from [12, 42] (middle panel) are compared to the LDA+DMFT estimate of the spectra (green line). A Gaussian broadening (FWHM 0.2 eV) is added to simulate the instrument resolution. The LDA+DMFT total DOS, subject to the same broadening, is shown for comparison (dotted line). In the right panel, we plot the orbital-resolved DOS without broadening (5f in red, sum of all others in dotted blue). All theoretical lines correspond to the [210] ferromagnet ($\Delta_{fd} = 35$ meV).

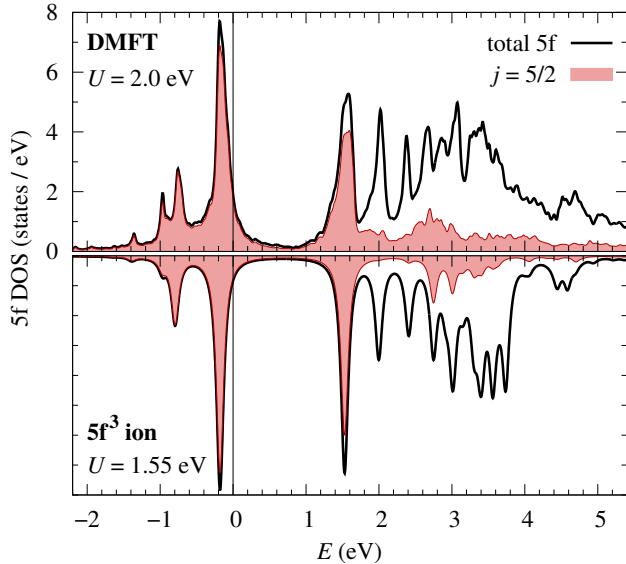


FIG. 8. The uranium 5f DOS in the [210] ferromagnet from the LDA+DMFT method ($\Delta_{fd} = 35$ meV) in the top panel is compared to the DOS from an atomic calculation ($5f^3$ state) in the bottom panel (black lines). The parameter $F_0 = U$ was reduced in the atomic calculation to mimic the screening effects incorporated in the LDA+DMFT method. The $j = 5/2$ components of the 5f DOS are shown in red.

the ionic model is reduced to 1.55 eV compared to 2.0 eV in LDA+DMFT. The higher Slater parameters F_k and the spin-orbit parameter ζ are identical. This observation indicates that the 5f states in the LDA+DMFT are very close to being fully localized, only their Coulomb repulsion is screened more than it would be in the fully localized Hubbard-I approximation. In addition, Fig. 8 also shows

the $j = 5/2$ component of the 5f DOS to be compared with the shape of the M_4 absorption line [13].

Finally, in Fig. 9 we present the momentum-resolved 5f spectral density along high-symmetry directions in the Brillouin zone. We compare different models for the electronic correlations, namely LSDA, LSDA+ U and LSDA+DMFT, in the ferromagnetic state with magnetic moments pointing along the [210] direction. The [001] ferromagnetic state differs only in minor details. When the Hubbard term is included (LSDA+ U and LSDA+DMFT), a gap between the occupied and unoccupied 5f bands appears and the occupied 5f states move slightly away from the Fermi level. Given the same interaction parameters (U and J , or F_k), this gap is larger in LSDA+ U , which indicates that the screening of the Coulomb parameters is stronger in LSDA+DMFT than in LSDA+ U . The situation is analogous to Fig. 8 since the U -induced potential in LSDA+ U has the form of a *ionic* Hartree-Fock approximation. Another difference between the LSDA+DMFT and LSDA+ U electronic structure is the incoherent character of the 5f states visible in the LSDA+DMFT solution, starting approximately 2.5 eV above the Fermi level.

C. Sommerfeld coefficient

Figure 9 illustrates that the Fermi level cuts right through the 5f bands in LSDA, which is accompanied by a high density of states at the Fermi level and, subsequently, by a large Sommerfeld coefficient of the electronic specific heat γ . Indeed, LSDA predicts $\gamma > 20$ mJ/mol·K² (Table II), which is at odds with the experimental value 11 mJ/mol·K² [9]. In DFT+DMFT (and in LSDA+ U as well), the 5f states move away from the Fermi level toward higher binding energies and the coefficient γ is re-

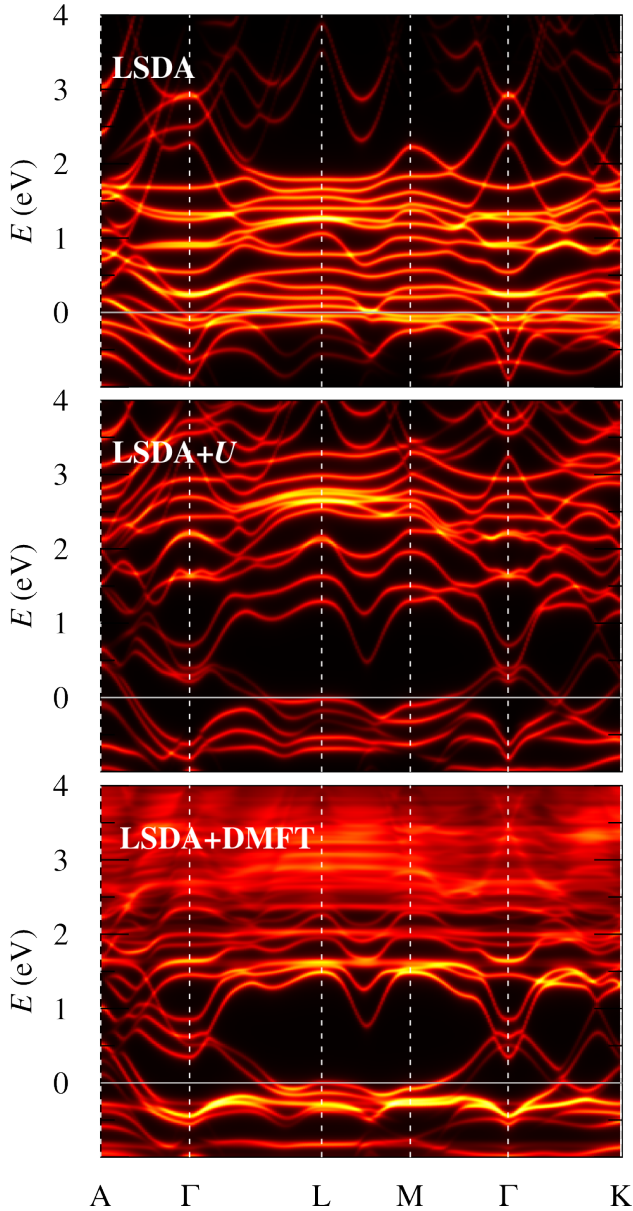


FIG. 9. Momentum-resolved 5f spectral density. The electronic correlations are described with increasing level of sophistication from top to bottom: LSDA, LSDA+ U ($U = 2.0$ eV, $J = 0.59$ eV and the FLL double counting), and LSDA+DMFT (the same interaction parameters, and $U_H = 3.3$ eV and $\Delta_{fd} = 35$ meV). The [210] ferromagnetic state is shown in all three panels. The same U and J produce a larger gap between the occupied and unoccupied 5f states in LSDA+ U than in LSDA+DMFT.

duced to approximately $8 \text{ mJ/mol}\cdot\text{K}^2$ (Table II), yielding a considerably better agreement with experiments. The computed Sommerfeld coefficient should be smaller than observed in experiments since we do not take into account any enhancement due to phonons. We do not observe much variation of γ when changing the orientation of the magnetic moments or when alternating the parent band structure (Table II).

IV. CONCLUSIONS

We have studied the electronic structure and magnetic properties of the ferromagnetic compound UGa_2 using the DFT+DMFT method, and compared our results with more approximate electronic-structure methods. We have found that our implementation of the DFT+DMFT method reproduces the experimentally observed large magnetic moments as well as the sign of the magnetocrystalline anisotropy energy, when the exchange interaction between uranium 6d and 5f states is included in a semi-empirical manner. This is done either in the form of an extra potential acting on the 5f states or in the form of a spin-polarized double-counting correction. We have compared two formulations of the DFT+DMFT method, one keeping the non-5f states spin restricted (LDA), and the other allowing their spin polarization (LSDA). Of the two, the LDA-based variant was found to provide more consistent results. It is a future work to investigate how the semi-empirical approach to the 6d-5f exchange could be improved toward a fully first-principles method.

Besides the magnetic properties, we have also modeled the valence-band photoemission spectra on the basis of the DFT+DMFT density of states. We were not able to fully explain the differences between the two published photoemission experiments [11, 12] but we could understand how the electron-electron correlations move the 5f states slightly away from the Fermi level, which is in accord with both photoemission spectra as well as with the observed small Sommerfeld coefficient of the electronic specific heat. With the aid of the DFT+DMFT method, it is thus possible to reconcile large magnetic moments and a small Sommerfeld coefficient with the 5f spectral density in the close vicinity of the Fermi level.

Our calculations indicate a close-to-localized uranium 5f states in UGa_2 . From the comparison to the experimental photoemission spectra we deduce that the tendency to localization is probably slightly overestimated in our theoretical description. Such a tendency is to be expected for the employed impurity solver that implements a form of expansion around the atomic limit.

ACKNOWLEDGMENTS

The work was supported by the Czech Science Foundation under the grants No. 18-02344S and No. 21-09766S. We thank S.-i. Fujimori for experimental data, and L. Havela, J. Kuneš and A. B. Shick for fruitful discussions. Computational resources were partially supplied by the project “e-Infrastruktura CZ” (e-INFRA LM2018140) provided within the program Projects of Large Research, Development and Innovations Infrastructures.

Appendix A: Parameters of DFT calculations

To perform all DFT calculations presented in this paper, we employed the WIEN2k package [24] that implements linearized augmented plane-wave method and its extensions. It combines a scalar-relativistic description with spin-orbit coupling [25]. All calculations were performed at the experimental lattice constants $a = 4.213 \text{ \AA}$ and $c = 4.020 \text{ \AA}$, reported in [3], with the following parameters: the radii of the muffin-tin spheres were $R_{\text{MT}}(\text{U}) = 2.80 a_B$ for uranium atoms and $R_{\text{MT}}(\text{Ga}) = 2.25 a_B$ for gallium atoms, the Brillouin zone was sampled with 6137 k points (900 k points in the irreducible wedge), and the basis-set cutoff K_{max} was defined with $R_{\text{MT}}(\text{Ga}) \times K_{\text{max}} = 10.0$. The default basis set with local orbitals for semicore states (U 6s, 6p, and Ga 3d) was used in all cases.

In Table III, we list the orbital and spin magnetic moments of the uranium 5f shell, the total magnetic moment of the unit cell, the filling of the 5f shell, and the Sommerfeld coefficient for three ferromagnetic states with moments pointing along different crystallographic axes. The moments and the filling of the 5f shell correspond to the muffin-tin sphere, they can be compared to the values computed for the maximally localized Wannier functions shown in Table II. The largest components of the total moment quoted in Table III are the 5f moments, a sizable contributions come also from the spin moments in the U 6d states ($\approx -0.1 \mu_B$) and in the interstitial ($\approx -0.2 \mu_B$). The moments induced at Ga atoms are negligible.

The maximally localized Wannier functions for the DMFT calculations were found with the Wannier90 code [27]. The spread minimization was performed on $16 \times 16 \times 16$ mesh of k points. Since there are no gaps in the spectrum above the Fermi level, disentanglement was necessary [44]. We used 62 Bloch states on input, which corresponds to the energy window from -10 eV to 24 eV . (Our largest tight-binding models, that is, those actually used for the DMFT calculations, have 48 Wannier functions). The frozen inner window extended to 6 eV (3 eV for the smallest model listed in Table I), going higher meant that the centers of the Wannier functions started drifting away from the atomic centers, which is undesirable in

TABLE III. The orbital and spin magnetic moments in uranium 5f shell, m_S and m_L (in μ_B), the total magnetic moment in the unit cell m_{tot} (in μ_B), the occupation of the 5f shell n_f , and the Sommerfeld coefficient γ (in $\text{mJ/mol}\cdot\text{K}^2$). The 5f magnetic moments and the 5f filling correspond to the atomic (muffin-tin) spheres.

| | direction | m_S | m_L | m_{tot} | n_f | γ |
|------|-----------|-------|-------|------------------|-------|----------|
| LDA | – | – | – | – | 2.45 | 43.9 |
| LSDA | [100] | –1.82 | 2.67 | 0.57 | 2.51 | 24.7 |
| LSDA | [210] | –1.82 | 2.64 | 0.54 | 2.50 | 26.7 |
| LSDA | [001] | –1.86 | 2.72 | 0.57 | 2.50 | 22.5 |

our application that assumes the Wannier functions to be atomic-like. In the model used for the DMFT calculations, the original WIEN2k bands were represented perfectly up to 6 eV above the Fermi level, the match was still very good up to approximately 12 eV , and above that the correspondence quickly deteriorated.

Appendix B: Construction of the impurity model

Here we discuss how the parameters of the finite impurity model, Eq. (1), are found so that the model matches the effective medium (the bath) as closely as possible. The impurity Hamiltonian has the form a block matrix

$$\mathbb{H}_{\text{imp}} = \begin{pmatrix} \mathbb{H}_{\text{loc}} & \mathbb{V}_1 & \mathbb{V}_2 & \mathbb{V}_3 & \cdots \\ \mathbb{V}_1^\dagger & \mathbb{H}_{\text{bath}}^{(1)} & 0 & 0 & \cdots \\ \mathbb{V}_2^\dagger & 0 & \mathbb{H}_{\text{bath}}^{(2)} & 0 & \cdots \\ \mathbb{V}_3^\dagger & 0 & 0 & \mathbb{H}_{\text{bath}}^{(3)} & \cdots \\ \vdots & \vdots & \vdots & \vdots & \ddots \end{pmatrix}, \quad (\text{B1})$$

where all blocks are 14×14 square matrices. The local Hamiltonian \mathbb{H}_{loc} contains a strong spin-orbit coupling which does not commute with the hybridization function that follows the crystal symmetry. Therefore, the problem cannot be simplified to diagonal matrices.

If there is only one \mathbb{H}_{bath} block, all three matrices \mathbb{H}_{loc} , \mathbb{H}_{bath} and \mathbb{V} can be determined by comparing the large z asymptotics of the local block of the impurity Green's function,

$$\mathbb{G}_{\text{loc}}(z) = \left[z\mathbb{I} - \mathbb{H}_{\text{loc}} - \sum_i \mathbb{V}_i (z\mathbb{I} - \mathbb{H}_{\text{bath}}^{(i)})^{-1} \mathbb{V}_i^\dagger \right]^{-1}, \quad (\text{B2})$$

to the asymptotics of the bath Green's function defined as

$$\mathbb{G}(z) = [G_f^{-1}(z) + \Sigma(z)]^{-1}. \quad (\text{B3})$$

Here $G_f(z)$ is the 5f block of the local Green's function $G(z)$ from Eq. (6). We refer the reader to [32] for details. For larger impurity models, like Eq. (B1), this strategy leads to an unsolvable set of polynomial equations for the 14×14 square matrices. To overcome the problem, we combine two shorter asymptotic expansions, one for the Green's function as before, and one for the hybridization function.

The asymptotic expansion of the local block of the impurity Green's function $\mathbb{G}_{\text{loc}}(z)$ starts as

$$\mathbb{G}_{\text{loc}}(z) = \frac{\mathbb{I}}{z} + \frac{\mathbb{H}_{\text{loc}}}{z^2} + O(z^{-3}), \quad (\text{B4})$$

and the analogous expansion of the hybridization function

$$\Delta_{\text{imp}} = z\mathbb{I} - \mathbb{H}_{\text{loc}} - \mathbb{G}_{\text{loc}}^{-1}(z) \quad (\text{B5})$$

starts as

$$\Delta_{\text{imp}} = \sum_i \mathbb{V}_i (z\mathbb{I} - \mathbb{H}_{\text{bath}}^{(i)})^{-1} \mathbb{V}_i^\dagger = \sum_i \left[\frac{\mathbb{V}_i \mathbb{V}_i^\dagger}{z} + \frac{\mathbb{V}_i \mathbb{H}_{\text{bath}}^{(i)} \mathbb{V}_i^\dagger}{z^2} \right] + O(z^{-3}). \quad (\text{B6})$$

From the other side, the bath Green's function, Eq. (B3), reads in the spectral representation as

$$\mathbb{G}(z) = \int \frac{\mathbb{A}(\epsilon)}{z - \epsilon} d\epsilon, \quad (\text{B7})$$

where we introduced the spectral density

$$\mathbb{A}(\epsilon) = \frac{\mathbb{G}(\epsilon - i0) - \mathbb{G}(\epsilon + i0)}{2\pi i}. \quad (\text{B8})$$

The asymptotic expansion of the bath Green's function is obtained by expanding the denominator in Eq. (B7),

$$\mathbb{G}(z) = \sum_{n=0}^{\infty} \frac{\mathbb{M}_n}{z^{n+1}}, \quad \mathbb{M}_n = \int \epsilon^n \mathbb{A}(\epsilon) d\epsilon, \quad (\text{B9})$$

where \mathbb{M}_n are moments of the spectral density. The spectral density $\mathbb{A}(\epsilon)$ is a hermitian matrix and hence its moments are hermitian matrices as well. We immediately see that

$$\mathbb{H}_{\text{loc}} = \mathbb{M}_1. \quad (\text{B10})$$

The spectral representation of the hybridization function corresponding to $\mathbb{G}(z)$, that is, of $\Delta(z) = z\mathbb{I} - \mathbb{M}_1 - \mathbb{G}^{-1}(z)$, can be written as

$$\Delta(z) = \int \frac{\mathbb{B}(\epsilon)}{z - \epsilon} d\epsilon, \quad (\text{B11})$$

where the spectral density is defined as

$$\mathbb{B}(\epsilon) = \frac{\Delta(\epsilon - i0) - \Delta(\epsilon + i0)}{2\pi i}. \quad (\text{B12})$$

Now we split the support of $\mathbb{B}(\epsilon)$ to as many segments as many $\mathbb{H}_{\text{bath}}^{(i)}$ blocks we wish (or can afford) to have,

$$\Delta(z) = \sum_i \Delta_i(z), \quad \text{where } \Delta_i(z) = \int_{\epsilon_i}^{\epsilon_{i+1}} \frac{\mathbb{B}(\epsilon)}{z - \epsilon} d\epsilon \quad (\text{B13})$$

with $\epsilon_i < \epsilon_{i+1}$, and we pair each Δ_i with one summand in Eq. (B6). The splitting can be arbitrary or it can be guided by an insight into the structure of the hybridization function – the individual $\mathbb{H}_{\text{bath}}^{(i)}$ blocks can be aligned with groups of bands. In UGa_2 , the hybridization below the Fermi level comes mainly from Ga 4s and 4p bands, and in the first ≈ 6 eV above the Fermi level it is dominated by U 6d bands.

The asymptotic expansion at the individual intervals reads as

$$\Delta_i(z) = \sum_{n=0}^{\infty} \frac{\mathbb{N}_n^{(i)}}{z^{n+1}}, \quad \mathbb{N}_n^{(i)} = \int_{\epsilon_i}^{\epsilon_{i+1}} \epsilon^n \mathbb{B}(\epsilon) d\epsilon. \quad (\text{B14})$$

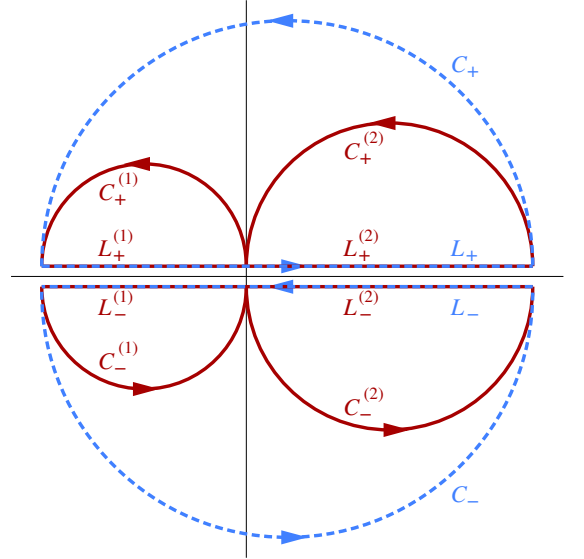


FIG. 10. Contours in the complex plane used for integration of the moments \mathbb{M}_1 (dashed blue) and $\mathbb{N}_n^{(i)}$ (red). Line segments are denoted as L_{\pm} , half circles as C_{\pm} .

Comparing Eqs. (B6) and (B14), the blocks of \mathbb{H}_{imp} can be written in terms of the moments $\mathbb{N}_n^{(i)}$ as

$$\mathbb{V}_i = \mathbb{V}_i^\dagger = \sqrt{\mathbb{N}_0^{(i)}}, \quad (\text{B15a})$$

$$\mathbb{H}_{\text{bath}}^{(i)} = \mathbb{V}^{-1} \mathbb{N}_1^{(i)} (\mathbb{V}^\dagger)^{-1}, \quad (\text{B15b})$$

which, together with Eq. (B10), concludes the construction of the impurity model \mathbb{H}_{imp} from the local Green's function $G(z)$. Optionally, we can diagonalize the blocks $\mathbb{H}_{\text{bath}}^{(i)}$ to make their interpretation more straightforward and to arrive at the form of the impurity model used in Eq. (1). The corresponding transformations are

$$\mathbb{H}_{\text{bath}}^{(i)} \rightarrow \mathbb{C}_i^{-1} \mathbb{H}_{\text{bath}}^{(i)} \mathbb{C}_i, \quad \mathbb{V}_i \rightarrow \mathbb{V}_i \mathbb{C}_i, \quad (\text{B16})$$

where \mathbb{C}_i are the appropriate unitary matrices and the new \mathbb{V}_i are no longer hermitian. By construction, the eigenvalues of $\mathbb{H}_{\text{bath}}^{(i)}$ are confined to intervals $(\epsilon_i, \epsilon_{i+1})$.

For the purpose of their actual evaluation, the moments are expressed in terms of contour integrals in the complex plane. Using the path segments sketched in Fig. 10, we have

$$\begin{aligned} \mathbb{M}_1 &= \frac{1}{2\pi i} \left[\int_{-L_-} - \int_{L_+} \right] z \mathbb{G}(z) dz \\ &= \frac{1}{2\pi i} \left[\int_{C_-} + \int_{C_+} \right] z \mathbb{G}(z) dz, \end{aligned} \quad (\text{B17})$$

$$\begin{aligned} \mathbb{N}_n^{(i)} &= \frac{1}{2\pi i} \left[\int_{-L_-^{(i)}} - \int_{L_+^{(i)}} \right] z^n [z\mathbb{I} - \mathbb{M}_1 - \mathbb{G}^{-1}(z)] dz \\ &= \frac{1}{2\pi i} \left[\int_{C_-^{(i)}} + \int_{C_+^{(i)}} \right] z^n [z\mathbb{I} - \mathbb{M}_1 - \mathbb{G}^{-1}(z)] dz, \end{aligned} \quad (\text{B18})$$

where the integral over the (dashed blue) circle $C = C_- \cap C_+$ encloses the entire support of $\mathbb{A}(\epsilon)$ and the integrals over the (red) circles $C^{(i)} = C_-^{(i)} \cap C_+^{(i)}$ enclose the intervals $(\epsilon_i, \epsilon_{i+1})$. During the DMFT calculations, the self-energy is thus evaluated along the circles C and $C^{(i)}$, and also along one additional semicircle in the upper half plane to compute the number of electrons in the primitive cell and to adjust the Fermi level. An alternative to the circle C , which serves for evaluation of $\mathbb{H}_{\text{loc}} = \mathbb{M}_1$, is described in Appendix C.

In the DFT+DMFT calculations of UGa₂ discussed in the paper, we used three intervals $(\epsilon_i, \epsilon_{i+1})$, namely $(-10, 0)$ eV, $(0, 6)$ eV and $(6, 12)$ eV. The hybridization above 12 eV was discarded, since our tight-binding Hamiltonians do not accurately represent the original DFT bands that far above the Fermi level (Appendix A).

Appendix C: Asymptotics of the bath Green's function and the local Hamiltonian

At each \mathbf{k} point, the tight-binding Hamiltonian $\hat{H}_{\mathbf{k}}$ can be divided into four blocks,

$$\hat{H}_{\mathbf{k}} = \begin{pmatrix} \hat{H}_{\mathbf{k}}^f & \hat{T}_{\mathbf{k}} \\ \hat{T}_{\mathbf{k}}^\dagger & \hat{H}_{\mathbf{k}}^{spd} \end{pmatrix}, \quad (\text{C1})$$

and the 5f block of the lattice Green's function can be written as

$$\hat{G}_{\mathbf{k}}^f(z) = \left[z\hat{I} - \hat{H}_{\mathbf{k}}^f - \hat{\Sigma}(z) - \hat{T}_{\mathbf{k}}(z\hat{I} - \hat{H}_{\mathbf{k}}^{spd})^{-1}\hat{T}_{\mathbf{k}}^\dagger \right]^{-1}. \quad (\text{C2})$$

Its asymptotic expansion reads as

$$\hat{G}_{\mathbf{k}}^f(z) = \frac{\hat{I}}{z} + \frac{\hat{H}_{\mathbf{k}}^f + \hat{\Sigma}(\infty)}{z^2} + O(z^{-3}), \quad (\text{C3})$$

where $\hat{\Sigma}(\infty)$ is the static part of the self-energy, which is the leading term of the expansion $\hat{\Sigma}(z) = \hat{\Sigma}(\infty) + O(z^{-1})$. For the bath Green's function, Eq. (B3), we need only the local element,

$$\begin{aligned} \hat{G}_f(z) &= \frac{1}{N} \sum_{\mathbf{k}} \hat{G}_{\mathbf{k}}^f(z) \\ &= \frac{\hat{I}}{z} + \frac{N^{-1} \sum_{\mathbf{k}} \hat{H}_{\mathbf{k}}^f + \hat{\Sigma}(\infty)}{z^2} + O(z^{-3}), \end{aligned} \quad (\text{C4})$$

respectively its inverse,

$$\hat{G}_f^{-1}(z) = z\hat{I} - \frac{1}{N} \sum_{\mathbf{k}} \hat{H}_{\mathbf{k}}^f - \hat{\Sigma}(\infty) + O(z^{-1}). \quad (\text{C5})$$

Inserting this expression into the definition of the bath Green's function, Eq. (B3), yields

$$\mathbb{G}(z) = \frac{\hat{I}}{z} + \frac{1}{z^2} \frac{1}{N} \sum_{\mathbf{k}} \hat{H}_{\mathbf{k}}^f + O(z^{-1}). \quad (\text{C6})$$

The self-energy cancels out from the first moment of the corresponding spectral density, and the moment thus equals to the local block of the tight-binding Hamiltonian,

$$\mathbb{M}_1 = \frac{1}{N} \sum_{\mathbf{k}} \hat{H}_{\mathbf{k}}^f = \mathbb{H}_{\text{loc}}, \quad (\text{C7})$$

throughout the whole DMFT self-consistency loop.

To extract the individual contributions to the Hamiltonian shown in Eq. (2), we can exploit the orthogonality of operators \hat{I} , $\hat{\mathbf{I}} \cdot \hat{\mathbf{s}}$, $\hat{\mathbf{s}}$ and \hat{O}_{kq} as 14×14 matrices. We can write

$$\epsilon_f = \text{Tr}(\mathbb{H}_{\text{loc}})/14, \quad (\text{C8a})$$

$$\Delta_X^\alpha = \text{Tr}(\hat{s}_\alpha \mathbb{H}_{\text{loc}}) / \text{Tr}(\hat{s}_\alpha \hat{s}_\alpha), \quad \alpha = x, y, z, \quad (\text{C8b})$$

$$\zeta = \text{Tr}(\hat{\mathbf{I}} \cdot \hat{\mathbf{s}} \mathbb{H}_{\text{loc}}) / \text{Tr}(\hat{\mathbf{I}} \cdot \hat{\mathbf{s}} \hat{\mathbf{I}} \cdot \hat{\mathbf{s}}), \quad (\text{C8c})$$

$$B_{kq} = \text{Tr}(\hat{O}_{kq} \mathbb{H}_{\text{loc}}) / \text{Tr}(\hat{O}_{kq} \hat{O}_{kq}). \quad (\text{C8d})$$

In the case of spin-polarized electronic structure, spin-dependent crystal-field parameters can be introduced as

$$B_{kq}^\sigma = \text{Tr}(\hat{O}_{kq} \hat{P}_\sigma \mathbb{H}_{\text{loc}}) / \text{Tr}(\hat{O}_{kq} \hat{P}_\sigma \hat{O}_{kq} \hat{P}_\sigma), \quad (\text{C8e})$$

where \hat{P}_σ is a projector to spin σ . Since the operator \hat{O}_{kq} is spin-independent, it commutes with \hat{P}_σ and we can simplify the denominator as

$$\begin{aligned} \text{Tr}(\hat{O}_{kq} \hat{P}_\sigma \hat{O}_{kq} \hat{P}_\sigma) &= \text{Tr}(\hat{O}_{kq} \hat{O}_{kq} \hat{P}_\sigma \hat{P}_\sigma) \\ &= \text{Tr}(\hat{O}_{kq} \hat{O}_{kq} \hat{P}_\sigma) = \frac{1}{2} \text{Tr}(\hat{O}_{kq} \hat{O}_{kq}). \end{aligned} \quad (\text{C9})$$

Consequently, the parameters B_{kq} are averages of the spin-dependent parameters B_{kq}^σ ,

$$B_{kq} = \frac{1}{2} \sum_{\sigma} B_{kq}^\sigma. \quad (\text{C10})$$

The spin dependence of the crystal-field parameters derived from the LSDA band structure is substantial, which is illustrated in Table IV. Note that we do not attempt to remove the 5f self-interaction from the crystal-field potential [45, 46]. Nevertheless, the spin dependence would not disappear even if we did [46].

TABLE IV. Crystal-field parameters B_{kq}^σ , Eq. (C8e), derived from the LSDA tight-binding Hamiltonian (s,p,d,f model). Spin-restricted parameters B_{kq} computed from Eq. (C8d) are the same as shown in Table I.

| | B_{20} | B_{40} | B_{60} | B_{66} |
|------------------------------|----------|----------|----------|----------|
| ferromagnetic solution [001] | | | | |
| restricted | 3.72 | 0.0061 | -0.0043 | -0.052 |
| spin \uparrow | 1.75 | -0.0024 | 0.0017 | -0.107 |
| spin \downarrow | 5.68 | 0.0146 | -0.0100 | 0.003 |
| ferromagnetic solution [210] | | | | |
| restricted | 3.92 | 0.0262 | -0.0011 | -0.044 |
| spin \uparrow | 1.54 | 0.0111 | -0.0154 | -0.009 |
| spin \downarrow | 6.30 | 0.0414 | 0.0133 | -0.079 |

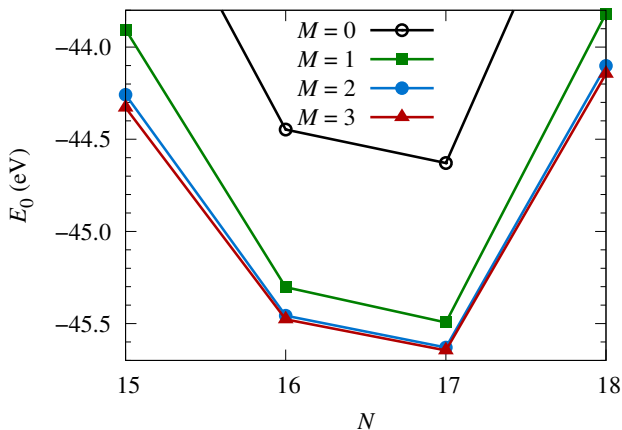


FIG. 11. The ground-state energy E_0 of the impurity model at different fillings N computed for increasing size of the many-body basis characterized by the cut-off M .

Appendix D: Convergence of the impurity-model solution with the size of the many-body basis

As indicated in Sec. II A, we cannot diagonalize the impurity model in the complete Fock space, only in reduced subspaces $\mathcal{H}_N^{(M)}$, defined in Eq. (5), where N is the number of electrons in the model (its filling) and M is a cut-off parameter. Analyzing the convergence of the complete DMFT solution with respect to M is computationally very demanding. Hence, we limit this Appendix to selected intermediate quantities, evaluation of which does not involve computing the self-energy. In particular, we diagonalize the auxiliary impurity model corresponding to the [210] ferromagnetic LDA+DMFT solution, obtained for $\Delta_{fd} = 35$ meV and presented in Sec. III, for different settings of the cut-off parameter M . The crudest approximation is $M = 0$ that does not allow any hops of electrons between the 5f shell and the bath, and thus corresponds to the Hubbard-I approximation. The best approximation we consider is $M = 3$, one step better than the setting employed in the main text.

Figure 11 shows the M -dependence of the ground-state energy E_0 for fillings N around the overall grandcanonical ground state which is located at $N = 17$. The differences between the $M = 2$ and $M = 3$ basis sets are very small (less than 70 meV), which indicates that $M = 2$ is indeed

a sensible choice. The differences are even smaller (less than 30 meV) for energy gaps $E_0(N \pm 1) - E_0(N)$ that determine the positions of the main peaks in the valence-band spectra like those plotted in Fig. 8.

Furthermore, we present the 5f occupation number $N_f = \text{Tr}(\hat{N}_f \hat{\rho})$, where $\hat{\rho}$ is the grandcanonical density matrix of the impurity model, together with its fluctuation

$$\Delta N_f = \sqrt{\text{Tr}(\hat{N}_f^2 \hat{\rho}) - N_f^2} \quad (\text{D1})$$

as functions of the cut-off M in Fig. 12. Both these quantities again change very little when M is increased from $M = 2$ to $M = 3$, which represents another reassurance that $M = 2$ is good enough.

Note that N_f should be the same number as n_f defined in Eq. (8) and listed in Table II, which follows from the DMFT embedding condition. In our DMFT calculations, they are not the same, N_f is approximately 0.2 larger than n_f , which is a consequence of the approximate finite impurity model (discrete bath) being used instead of the exact infinite impurity model (continuous bath). This is roughly the same discrepancy as we observed earlier when we applied this method to the ferromagnetic nickel [47]. In principle, the situation could be improved by adding more bath orbitals, but in practice, it is computationally prohibitive at present.

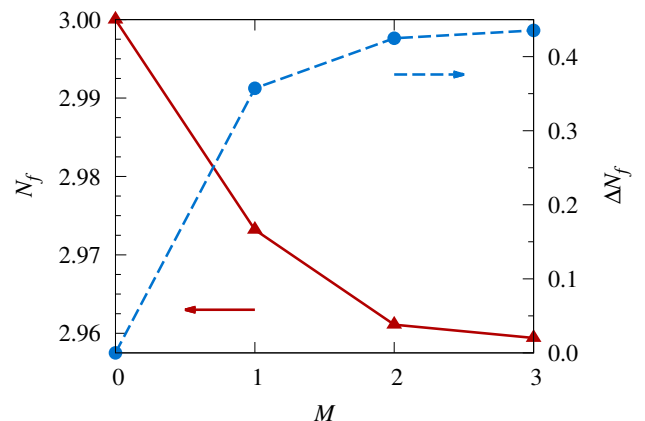


FIG. 12. Convergence of the 5f occupation number N_f (red triangles, left axis) and its fluctuation ΔN_f (blue circles, right axis) with respect to the basis-set cut-off M .

* kolorenc@fzu.cz

- [1] K. T. Moore and G. van der Laan, Nature of the 5f states in actinide metals, Rev. Mod. Phys. **81**, 235 (2009), arXiv:0807.0416 [cond-mat.str-el].
- [2] H. H. Hill, in *Plutonium 1970 and other Actinides*, edited by W. N. Miner (The Metallurgical Society of the AIME, New York, 1970) p. 2.
- [3] A. V. Andreev, K. P. Belov, A. V. Deryagin, Z. A. Kazei, R. Z. Levitin, A. Meňovský, Yu. F. Popov, and V. I.

Silant'ev, Crystal structure, and magnetic and magnetoelastic properties of UGa₂, Sov. Phys. JETP **48**, 1187 (1978).

- [4] A. V. Kolomiets, J.-C. Griveau, J. Prchal, A. V. Andreev, and L. Havela, Variations of magnetic properties of UGa₂ under pressure, Phys. Rev. B **91**, 064405 (2015), arXiv:1502.04948 [cond-mat.str-el].
- [5] A. C. Lawson, A. Williams, J. L. Smith, P. A. Seeger, J. A. Goldstone, J. A. O'Rourke, and Z. Fisk, Magnetic

- neutron diffraction study of UGa_3 and UGa_2 , *J. Magn. Magn. Mater.* **50**, 83 (1985).
- [6] R. Ballou, A. V. Deriagin, F. Givord, R. Lemaire, R. Z. Levitin, and F. Tasset, U^{4+} form factor in UGa_2 , *J. Phys. Colloques* **43**, C7–279 (1982).
 - [7] J.-M. Fournier and R. Troc, in *Handbook on the Physics and Chemistry of the Actinides*, Vol. 2, edited by A. Freeman and G. Lander (North Holland, Amsterdam, 1985) p. 35.
 - [8] R. J. Radwański and N. H. Kim-Ngan, The crystal-field and exchange interactions in UGa_2 , *J. Magn. Magn. Mater.* **140–144**, 1373 (1995).
 - [9] T. Honma, Y. Inada, R. Settai, S. Araki, Y. Tokiwa, T. Takeuchi, H. Sugawara, H. Sato, K. Kuwahara, M. Yokoyama, H. Amitsuka, T. Sakakibara, E. Yamamoto, Y. Haga, A. Nakamura, H. Harima, H. Yamagami, and Y. Ōnuki, Magnetic and Fermi surface properties of the ferromagnetic compound UGa_2 , *J. Phys. Soc. Japan* **69**, 2647 (2000).
 - [10] Y. Fujimaki, K. Satoh, and Y. Ōnuki, Superconductivity in LaGa_2 , *J. Phys. Soc. Japan* **61**, 395 (1992).
 - [11] T. Gouder, L. Havela, M. Diviš, J. Rebizant, P. M. Oppeneer, and M. Richter, Surface electronic structure of UGa_x films, *J. Alloys Compd.* **314**, 7 (2001).
 - [12] S.-i. Fujimori, M. Kobata, Y. Takeda, T. Okane, Y. Saitoh, A. Fujimori, H. Yamagami, Y. Haga, E. Yamamoto, and Y. Ōnuki, Manifestation of electron correlation effect in $5f$ states of uranium compounds revealed by $4d$ – $5f$ resonant photoelectron spectroscopy, *Phys. Rev. B* **99**, 035109 (2019), arXiv:1901.00956 [cond-mat.str-el].
 - [13] A. V. Kolomiets, M. Paukov, J. Valenta, B. Chatterjee, A. V. Andreev, K. O. Kvashnina, F. Wilhelm, A. Rogalev, D. Drozdenko, P. Minarik, J. Kolorenč, M. Richter, J. Prchal, and L. Havela, $5f$ states in UGa_2 probed by x-ray spectroscopies, *Phys. Rev. B* **104**, 045119 (2021).
 - [14] M. Diviš, M. Richter, H. Eschrig, and L. Steinbeck, *Ab initio* electronic structure, magnetism, and magnetocrystalline anisotropy of UGa_2 , *Phys. Rev. B* **53**, 9658 (1996).
 - [15] B. Chatterjee and J. Kolorenč, Magnetism and magnetic anisotropy in UGa_2 , *MRS Advances* **5**, 2639 (2020).
 - [16] V. I. Anisimov, F. Aryasetiawan, and A. I. Lichtenstein, First-principles calculations of the electronic structure and spectra of strongly correlated systems: the LDA + U method, *J. Phys.: Condens. Matter* **9**, 767 (1997).
 - [17] M.-T. Suzuki, N. Magnani, and P. M. Oppeneer, Microscopic theory of the insulating electronic ground states of the actinide dioxides AnO_2 ($\text{An} = \text{U}, \text{Np}, \text{Pu}, \text{Am}, \text{and Cm}$), *Phys. Rev. B* **88**, 195146 (2013), arXiv:1305.5627 [cond-mat.str-el].
 - [18] R. Qiu, B. Ao, and L. Huang, Effective Coulomb interaction in actinides from linear response approach, *Comp. Mater. Sci.* **171**, 109270 (2020), arXiv:1810.05859 [cond-mat.mtrl-sci].
 - [19] V. N. Antonov, B. N. Harmon, and A. N. Yaresko, Electronic structure and magneto-optical Kerr effect in UGa_2 , *J. Appl. Phys.* **94**, 7240 (2003).
 - [20] A. I. Lichtenstein and M. I. Katsnelson, *Ab initio* calculations of quasiparticle band structure in correlated systems: LDA++ approach, *Phys. Rev. B* **57**, 6884 (1998), arXiv:cond-mat/9707127 [cond-mat.str-el].
 - [21] G. Kotliar, S. Y. Savrasov, K. Haule, V. S. Oudovenko, O. Parcollet, and C. A. Marianetti, Electronic structure calculations with dynamical mean-field theory, *Rev. Mod. Phys.* **78**, 865 (2006), arXiv:cond-mat/0511085 [cond-mat.str-el].
 - [22] A. Georges, G. Kotliar, W. Krauth, and M. J. Rozenberg, Dynamical mean-field theory of strongly correlated fermion systems and the limit of infinite dimensions, *Rev. Mod. Phys.* **68**, 13 (1996), arXiv:cond-mat/9510091.
 - [23] M. I. Katsnelson and A. I. Lichtenstein, Electronic structure and magnetic properties of correlated metals, *Eur. Phys. J. B* **30**, 9 (2002), arXiv:cond-mat/0204564 [cond-mat.str-el].
 - [24] P. Blaha, K. Schwarz, F. Tran, R. Laskowski, G. K. H. Madsen, and L. D. Marks, WIEN2k: An APW+lo program for calculating the properties of solids, *J. Chem. Phys.* **152**, 074101 (2020).
 - [25] D. D. Koelling and B. N. Harmon, A technique for relativistic spin-polarised calculations, *J. Phys. C: Solid State Phys.* **10**, 3107 (1977).
 - [26] J. Kuneš, R. Arita, P. Wissgott, A. Toschi, H. Ikeda, and K. Held, Wien2wannier: From linearized augmented plane waves to maximally localized Wannier functions, *Comput. Phys. Commun.* **181**, 1888 (2010), arXiv:1004.3934 [cond-mat.mtrl-sci].
 - [27] A. A. Mostofi, J. R. Yates, Y.-S. Lee, I. Souza, D. Vanderbilt, and N. Marzari, wannier90: A tool for obtaining maximally-localised Wannier functions, *Comput. Phys. Commun.* **178**, 685 (2008), arXiv:0708.0650 [cond-mat.mtrl-sci].
 - [28] R. D. Cowan, *The theory of atomic structure and spectra* (University of California Press, Berkeley, 1981).
 - [29] H. Ogasawara, A. Kotani, and B. T. Thole, Calculation of magnetic x-ray dichroism in $4d$ and $5d$ absorption spectra of actinides, *Phys. Rev. B* **44**, 2169 (1991).
 - [30] H.-D. Meyer and S. Pal, A band-Lanczos method for computing matrix elements of a resolvent, *J. Chem. Phys.* **91**, 6195 (1989).
 - [31] A. Liebsch and H. Ishida, Temperature and bath size in exact diagonalization dynamical mean field theory, *J. Phys.: Condens. Matter* **24**, 053201 (2012), arXiv:1109.0158 [cond-mat.str-el].
 - [32] J. Kolorenč, A. B. Shick, and A. I. Lichtenstein, Electronic structure and core-level spectra of light actinide dioxides in the dynamical mean-field theory, *Phys. Rev. B* **92**, 085125 (2015), arXiv:1504.07979 [cond-mat.str-el].
 - [33] O. Gunnarsson and K. Schönhammer, Electron spectroscopies for Ce compounds in the impurity model, *Phys. Rev. B* **28**, 4315 (1983).
 - [34] L. V. Pourovskii, G. Kotliar, M. I. Katsnelson, and A. I. Lichtenstein, Dynamical mean-field theory investigation of specific heat and electronic structure of α - and δ -plutonium, *Phys. Rev. B* **75**, 235107 (2007), arXiv:cond-mat/0702342 [cond-mat.str-el].
 - [35] L. Peters, I. Di Marco, P. Thunström, M. I. Katsnelson, A. Kirilyuk, and O. Eriksson, Treatment of $4f$ states of the rare earths: The case study of TbN, *Phys. Rev. B* **89**, 205109 (2014), arXiv:1605.09538 [cond-mat.str-el].
 - [36] A. Shick and A. Lichtenstein, Electronic structure and magnetic properties of Dy adatom on Ir surface, *J. Magn. Magn. Mater.* **454**, 61 (2018).
 - [37] M. S. S. Brooks and B. Johansson, Exchange integral matrices and cohesive energies of transition metal atoms, *J. Phys. F: Met. Phys.* **13**, L197 (1983).
 - [38] I. V. Solovyev, P. H. Dederichs, and V. I. Anisimov, Corrected atomic limit in the local-density approximation and the electronic structure of d impurities in Rb, *Phys. Rev. B* **50**, 16861 (1994).

- [39] B. Amadon, F. Lechermann, A. Georges, F. Jollet, T. O. Wehling, and A. I. Lichtenstein, Plane-wave based electronic structure calculations for correlated materials using dynamical mean-field theory and projected local orbitals, *Phys. Rev. B* **77**, 205112 (2008), arXiv:0801.4353 [cond-mat.str-el].
- [40] L. Havela, S. Mašková, J. Kolorenč, E. Colineau, J.-C. Griveau, and R. Eloirdi, Electronic properties of Pu₁₉Os simulating β -Pu: the strongly correlated Pu phase, *J. Phys.: Condens. Matter* **30**, 085601 (2018).
- [41] We choose the [210] in-plane direction of magnetization instead of the experimental [100] direction due to technical limitation of our impurity solver. We have checked that this change does not significantly affect the ordered magnetic moments or the spectra in LSDA (Table III).
- [42] S.-i. Fujimori, private communication (2020).
- [43] J. Yeh and I. Lindau, Atomic subshell photoionization cross sections and asymmetry parameters: $1 \leq Z \leq 103$, *At. Data Nucl. Data Tables*. **32**, 1 (1985).
- [44] I. Souza, N. Marzari, and D. Vanderbilt, Maximally localized Wannier functions for entangled energy bands, *Phys. Rev. B* **65**, 035109 (2001), arXiv:cond-mat/0108084 [cond-mat.mtrl-sci].
- [45] P. Novák, K. Knížek, and J. Kuneš, Crystal field parameters with Wannier functions: Application to rare-earth aluminates, *Phys. Rev. B* **87**, 205139 (2013), arXiv:1303.1281 [cond-mat.str-el].
- [46] P. Delange, S. Biermann, T. Miyake, and L. Pourovskii, Crystal-field splittings in rare-earth-based hard magnets: An ab initio approach, *Phys. Rev. B* **96**, 155132 (2017), arXiv:1705.08027 [cond-mat.str-el].
- [47] J. Kolorenč, A. I. Poteryaev, and A. I. Lichtenstein, Valence-band satellite in ferromagnetic nickel: LDA+DMFT study with exact diagonalization, *Phys. Rev. B* **85**, 235136 (2012), arXiv:1202.6595 [cond-mat.mtrl-sci].